

Competition between charge-density-wave and superconductivity in the kagome metal  $\text{RbV}_3\text{Sb}_5$ 

N. N. Wang,<sup>1,2,\*</sup> K. Y. Chen<sup>①,1,2,\*</sup> Q. W. Yin,<sup>3,\*</sup> Y. N. N. Ma,<sup>1,2</sup> B. Y. Pan,<sup>4,1</sup> X. Yang,<sup>1,2</sup> X. Y. Ji,<sup>1,2</sup> S. L. Wu<sup>①,1,2</sup>  
 P. F. Shan,<sup>1,2</sup> S. X. Xu,<sup>1,2</sup> Z. J. Tu,<sup>3</sup> C. S. Gong,<sup>3</sup> G. T. Liu,<sup>1,2</sup> G. Li,<sup>1,2</sup> Y. Uwatoko,<sup>5</sup> X. L. Dong,<sup>1,2</sup> H. C. Lei,<sup>3,†</sup>  
 J. P. Sun<sup>①,1,2,‡</sup> and J.-G. Cheng<sup>①,1,2,§</sup>


<sup>1</sup>Beijing National Laboratory for Condensed Matter Physics and Institute of Physics, Chinese Academy of Sciences, Beijing 100190, China

<sup>2</sup>School of Physical Sciences, University of Chinese Academy of Sciences, Beijing 100190, China

<sup>3</sup>Department of Physics and Beijing Key Laboratory of Opto-electronic Functional Materials & Micro-nano Devices, Renmin University of China, Beijing 100872, China

<sup>4</sup>School of Physics and Optoelectronic Engineering, Ludong University, Yantai, Shandong 264025, China

<sup>5</sup>Institute for Solid State Physics, University of Tokyo, Kashiwa, Chiba 277-8581, Japan

 (Received 3 July 2021; revised 31 August 2021; accepted 8 September 2021; published 7 October 2021)

The interplay between charge-density-wave (CDW) order and superconductivity (SC) in the kagome metal  $\text{RbV}_3\text{Sb}_5$  is studied by tracking the evolutions of their transition temperatures  $T^*$  and  $T_c$  as a function of pressure ( $P$ ) via measurements of resistivity and magnetic susceptibility under various hydrostatic pressures up to  $\sim 5$  GPa. It is found that the CDW order at  $T^*$  experiences a subtle modification at  $P_{c1} \approx 1.5$  GPa before it is completely suppressed around  $P_{c2} \approx 2.4$  GPa. Accordingly, the superconducting transition  $T_c(P)$  exhibits a shallow M-shaped double superconducting dome with two extrema of  $T_c^{\text{onset}} \approx 4.4$  and 3.9 K around  $P_{c1}$  and  $P_{c2}$ , respectively, leading to a fourfold enhancement of  $T_c$  with respect to that at ambient pressure. The constructed  $T$ - $P$  phase diagram of  $\text{RbV}_3\text{Sb}_5$  resembles that of  $\text{CsV}_3\text{Sb}_5$  and shares similar features to many other unconventional superconducting systems with intertwined competing electronic orders. The strong competition between CDW and SC is also evidenced by the broad superconducting transition width in the coexistent region. Our results shed more light on the intriguing physics involving intertwined electronic orders in this topological kagome metal family.

DOI: [10.1103/PhysRevResearch.3.043018](https://doi.org/10.1103/PhysRevResearch.3.043018)

## I. INTRODUCTION

In the last decades, numerous research efforts have been devoted to exploring the interplay between superconductivity (SC) and various competing electronic orders in unconventional superconducting systems [1–10]. The recently discovered kagome metals  $\text{AV}_3\text{Sb}_5$  ( $A = \text{K}, \text{Rb}, \text{and Cs}$ ) fall into this category because they show the coexistence of charge-density-wave (CDW) order and SC in addition to the presence of nontrivial topological band structure [11–14]. The superconducting transition occurs at  $T_c = 0.93, 0.92,$  and  $2.5$  K, while the CDW order appears at  $T^* \approx 78, 104,$  and  $94$  K for  $\text{KV}_3\text{Sb}_5$  [13],  $\text{RbV}_3\text{Sb}_5$  [14], and  $\text{CsV}_3\text{Sb}_5$  [12], respectively, as revealed by resistivity, magnetization, specific heat, x-ray diffraction, optical spectroscopy, and scanning tunneling microscopy measurements [12–24]. Interestingly,

a chiral CDW state with breaking time-reversal symmetry has been observed in  $\text{AV}_3\text{Sb}_5$  and was critical for the emergence of giant anomalous Hall effect and unconventional SC [15,25]. Moreover, theoretical calculations on the kagome Hubbard model with different electron filling states have shown many exotic phases, including spinless fermions [26], valence-bond solid phases [27], CDW state [28–31], chiral spin-density-wave (SDW) state [28,32], exotic superconducting states [28,29,32–34], and topological point defects [35]. To elucidate the detailed interplay between the intertwined CDW order and SC, it is important to tune the electronic states of  $\text{AV}_3\text{Sb}_5$  by methods such as chemical doping, intercalation, or applying high pressures.

So far, several high-pressure studies have been performed on  $\text{KV}_3\text{Sb}_5$  and  $\text{CsV}_3\text{Sb}_5$  to unveil the intimated correlations between the CDW order and SC [36–41]. For  $\text{KV}_3\text{Sb}_5$ , the application of high pressure was found to enhance the superconducting transition temperature  $T_c$ , concomitant with the suppression of the CDW order, suggesting a strong competition between CDW and SC [38]. However, for  $\text{CsV}_3\text{Sb}_5$ , with much larger interlayer distance, detailed high-pressure transport measurements reveal a more complex relationship between CDW and SC, displaying an unusual M-shaped double superconducting dome accompanying a monotonic suppression of CDW order [36,41]. Such an unusual phase diagram of  $\text{CsV}_3\text{Sb}_5$  should arise from a subtle modification of the CDW order associated with the large compression of

\*These authors contributed equally to this paper.

<sup>†</sup>hlei@ruc.edu.cn

<sup>‡</sup>jpsun@iphy.ac.cn

<sup>§</sup>jpgcheng@iphy.ac.cn

interlayer distance, as indicated by density functional theory calculations [36]. The more dispersive band structure along the  $c$  axis for  $\text{KV}_3\text{Sb}_5$  with much reduced interlayer distance (or  $c$  axis) [11,42] can explain the rapid suppression of CDW order at a lower critical pressure of  $P_c \approx 0.4$  GPa [38]. Moreover, resistance measurements on  $\text{CsV}_3\text{Sb}_5$  by using diamond anvil cells over a more extended pressure range have uncovered the emergence of a second superconducting phase (SC-II) at  $P > 15$  GPa with a maximum  $T_c \approx 5$  K [37,39,40,43]. Since high-pressure x-ray diffraction rules out the occurrence of structural phase transition around this pressure [39], the observed SC-II phase at  $P > 15$  GPa has been attributed to a Lifshitz transition, as supported by the transport measurements and band structure calculations [37,39]. In comparison with K and Cs, Rb has an intermediate atomic radius, and consequently, the interlayer  $c$ -axis distance of  $\text{RbV}_3\text{Sb}_5$  lies between that of  $\text{KV}_3\text{Sb}_5$  and  $\text{CsV}_3\text{Sb}_5$  [14]. It is thus interesting to investigate the evolutions of CDW and SC in  $\text{RbV}_3\text{Sb}_5$  under hydrostatic pressures to gain a comprehensive understanding on the relationship between CDW order and SC in this class of kagome superconductors.

In this paper, we have performed detailed resistivity, direct-current (dc) field, and alternate-current (ac) field magnetic susceptibility measurements on  $\text{RbV}_3\text{Sb}_5$  single crystal by using the piston cylinder cell (PCC) and cubic anvil cell (CAC) under various hydrostatic pressures up to 5.2 GPa. Our results reveal a shallow M-shaped double superconducting dome in  $\text{RbV}_3\text{Sb}_5$ , which should correlate with the cryptic modification of the CDW order at  $P_{c1} \approx 1.5$  GPa before it is completely suppressed around  $P_{c2} \approx 2.4$  GPa. Moreover, the maximum  $T_c$  can be enhanced to  $\sim 4.4$  K at  $\sim 1.5$  GPa, a fourfold enhancement compared with  $T_c$  at ambient pressure. The constructed  $T$ - $P$  phase diagram, like that of  $\text{CsV}_3\text{Sb}_5$  [36], clearly reveals the competition between CDW and SC, providing more insights into the high-pressure properties of this topological kagome superconducting family.

## II. EXPERIMENTAL DETAILS

Single crystals of  $\text{RbV}_3\text{Sb}_5$  were synthesized by Rb ingot (purity 99.9%), V powder (purity 99.9%), and Sb grains (purity 99.999%) using the self-flux method [14]. Temperature dependences of resistivity and ac magnetic susceptibility for  $\text{RbV}_3\text{Sb}_5$  samples were measured simultaneously by using a self-clamped PCC under various hydrostatic pressures up to 2.2 GPa [44]. Here, we used the Daphne 7373 as the pressure transmitting medium (PTM) in PCC. The resistivity was measured with the standard four-probe method with the electrical current applied within the  $ab$  plane. The magnetic field was applied along the  $c$  axis. The ac susceptibility of  $\text{RbV}_3\text{Sb}_5$  together with a piece of Pb placed in the same coil was measured with the mutual induction method. An excitation current of  $\sim 1$  mA with a frequency of 1117 Hz was applied to the primary coil, and the output signal was picked up with a Stanford Research SR830 lock-in amplifier. The measured superconducting transition of Pb was used to determine the pressure value in PCC, and it was also used as a reference to estimate the superconducting shielding volume of the  $\text{RbV}_3\text{Sb}_5$ . We have also employed a palm-type CAC

to measure the resistivity of  $\text{RbV}_3\text{Sb}_5$  up to 5.2 GPa [45]. Glycerol was employed as the liquid PTM for CAC. Finally, we used a miniature BeCu PCC to measure the dc magnetization under various pressures up to 0.84 GPa in the commercial magnetic property measurement system (MPMS-3, Quantum Design). The  $\text{RbV}_3\text{Sb}_5$  crystals together with a piece of lead (Pb) were loaded into a Teflon capsule filled with Daphne 7373 as the PTM, and the pressure value was determined from the relative shift of the  $T_c$  of Pb. All measurements were performed in the zero-field-cooled (ZFC) mode.

## III. RESULTS AND DISCUSSIONS

Figure 1(a) shows the temperature dependence of the in-plane resistivity  $\rho(T)$  of  $\text{RbV}_3\text{Sb}_5$  single crystal at ambient pressure. The normal-state  $\rho(T)$  exhibits a typical metallic behavior with the residual resistivity ratio (RRR) =  $\rho(290 \text{ K})/\rho(1.5 \text{ K}) = 39$ , indicating the high quality of our samples. As can be seen, a kinklike anomaly appears in  $\rho(T)$  at  $T^* \approx 103$  K, as indicated by the downward arrow, and this feature is correlated with the formation of the CDW order [14]. An enlarged view of  $\rho(T) < 1.5$  K is depicted in the inset of Fig. 1(a), which shows that the superconducting transition starts at  $\sim 1.1$  K and reaches zero resistance at  $\sim 0.78$  K. Here, the  $T_c^{\text{onset}}$  is determined as the interception between two straight lines below and above the superconducting transition, and  $T_c^{\text{zero}}$  is defined as the zero-resistivity temperature. These results are consistent with the previous report [14]. Then we measure the field dependence of resistivity  $\rho(H)$  of  $\text{RbV}_3\text{Sb}_5$  at various temperatures up to 0.93 K with the field applied along the  $ab$  plane and the  $c$  axis, respectively, as shown in Figs. 1(b) and 1(c). We can see that the superconducting upper critical field  $\mu_0 H_{c2}$  is continuously shifted to lower fields with increasing temperature gradually. Here, we determined the upper critical field  $\mu_0 H_{c2}$  from the 90% drops of  $\rho(H)$  curves and plotted the temperature dependence of  $\mu_0 H_{c2}(T)$  in Fig. 1(d). As can be seen, the  $\mu_0 H_{c2}(T)$  can be well fitted by using the Ginzburg-Landau (GL) formula:  $\mu_0 H_{c2}(T) = \mu_0 H_{c2}(0) (1 - t^2)/(1 + t^2)$ , where  $\mu_0 H_{c2}(0)$  is defined as the zero-temperature upper critical field, and  $t$  represents the reduced temperature  $T/T_c$ . The calculated  $\mu_0 H_{c2}^{\parallel ab}(0)$  and  $\mu_0 H_{c2}^{\parallel c}(0)$  are 0.3 and 0.11 T, respectively. Moreover, the corresponding GL coherent lengths are estimated to be  $\xi_{\text{GL}}^{\parallel ab} = 547.0 \text{ \AA}$  and  $\xi_{\text{GL}}^{\parallel c} = 200.6 \text{ \AA}$  based on the formula  $\mu_0 H_{c2}^{\parallel c}(0) = \Phi_0/2\pi\xi_{\text{GL}}^{\parallel c}$  and  $\mu_0 H_{c2}^{\parallel ab}(0) = \Phi_0/2\pi\xi_{\text{GL}}^{\parallel ab}$ , where  $\Phi_0 = hc/2e$  is the magnetic flux quantum [46]. Therefore, the obtained anisotropy parameter is  $\gamma = \mu_0 H_{c2}^{\parallel ab}(0)/\mu_0 H_{c2}^{\parallel c}(0) \approx 2.73$ , which is  $\sim \frac{1}{3}$  of that in  $\text{CsV}_3\text{Sb}_5$  [47]. The reduced anisotropy is consistent with the reduced ionic radius of alkali metal from Cs to Rb. For the anisotropic superconductors, we can use the ratio  $\gamma = \sqrt{m_c^*/m_{ab}^*}$  to express the band structure anisotropy, where the  $m_c^*$  and  $m_{ab}^*$  are the effective mass of the quasiparticles along the  $c$  axis and within the  $ab$  plane, respectively. The estimated  $m_c^*/m_{ab}^* \sim 7.5$  indicates a relatively strong anisotropy of the band structure in  $\text{RbV}_3\text{Sb}_5$ .

To further characterize the superconducting transition of  $\text{RbV}_3\text{Sb}_5$ , we measured the low-temperature magnetization  $M(T)$  at a magnetic field of 5 Oe under ZFC and field-cooled

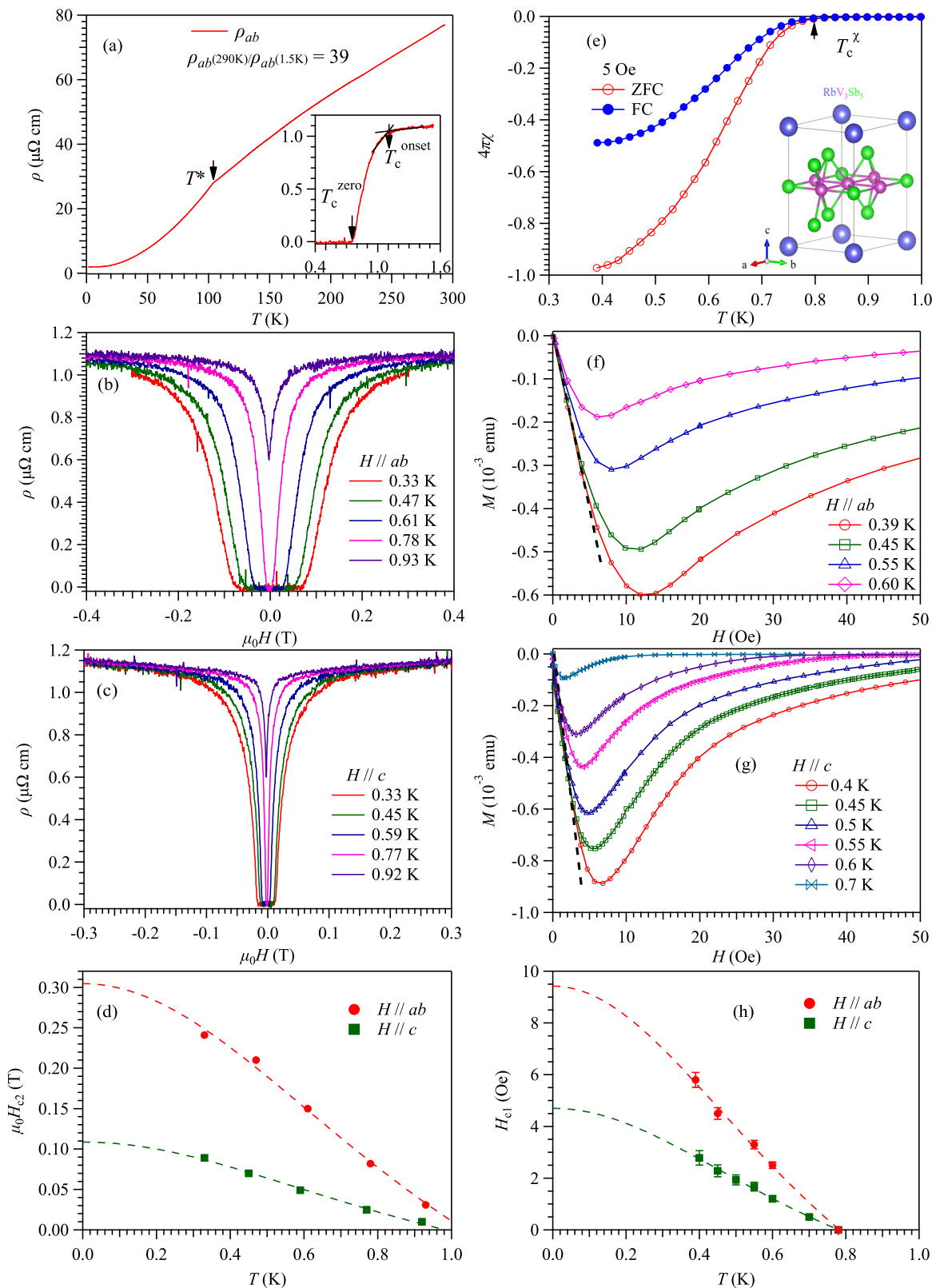


FIG. 1. (a) In-plane resistivity  $\rho(T)$  of RbV<sub>3</sub>Sb<sub>5</sub> at ambient pressure from 300 K down to 2 K. The inset shows the  $\rho(T) < 1.5$  K, highlighting the superconducting transition. (b) and (c) Field dependences of  $\rho(H)$  measured with field parallel to the  $ab$  plane and the  $c$  axis at various temperatures. (d) The anisotropic upper critical field  $\mu_0 H_{c2}$ , defined as the field at 90% of the normal-state resistivity. (e) The direct current (dc) magnetic susceptibilities under zero-field-cooled (ZFC) and field-cooled (FC) conditions. (f) and (g) Isothermal magnetization at various temperatures with magnetic field parallel to the  $ab$  plane and the  $c$  axis. (h) The anisotropic lower critical field  $\mu_0 H_{c1}$ , defined as the fields at which  $M$ - $H$  curves start to deviate from the linear line indicated by the dashed lines in (f) and (g).

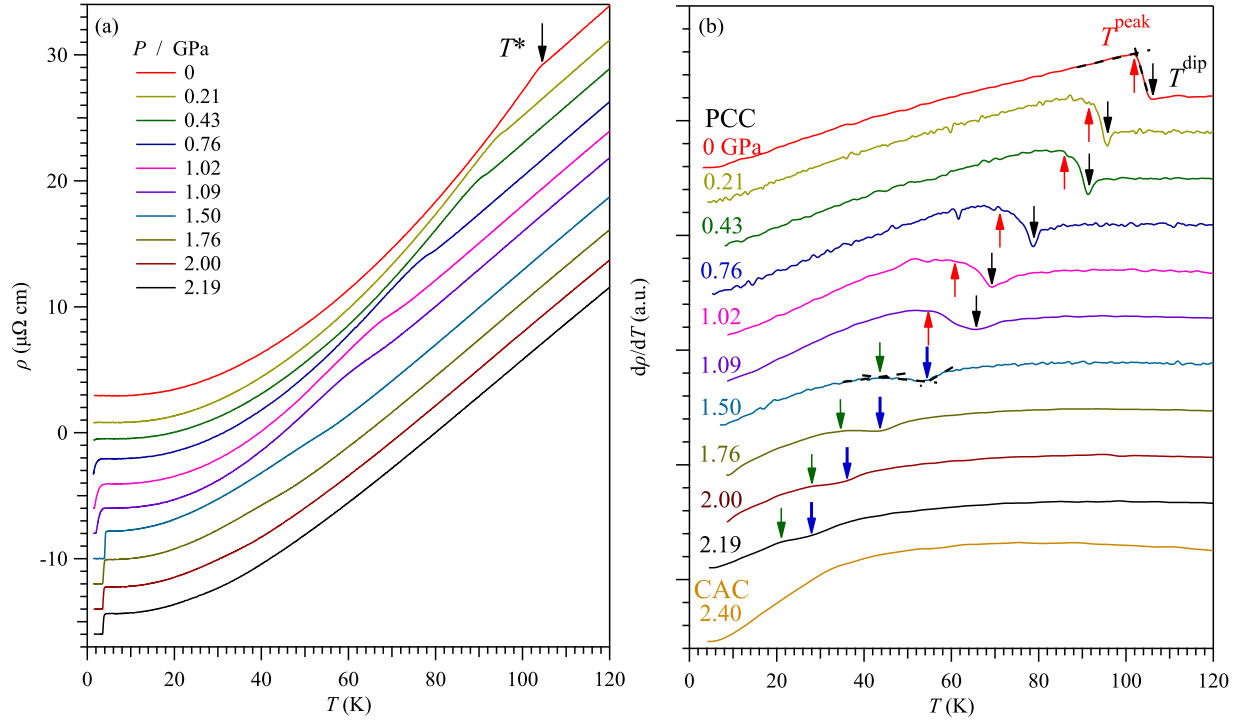


FIG. 2. Variation of the charge-order-related transition under high pressures. Temperature dependences of (a) resistivity  $\rho(T)$  and (b) its derivative  $d\rho/dT$  for the  $\text{RbV}_3\text{Sb}_5$  sample measured in a piston cylinder cell (PCC) under various pressures up to 2.19 GPa and in a cubic anvil cell (CAC) at 2.4 GPa. The charge-order or charge-density-wave (CDW)-like transition temperature  $T^*$  are marked by the arrows in the figures. The curves in (a) and (b) have been shifted vertically for clarity.

(FC) conditions. As shown in Fig. 1(e), the obvious diamagnetic signal can be seen in the ZFC and FC curves, and it reveals the bulk SC after correcting the demagnetization factor. The onset of superconducting transition appears at  $T_c \approx 0.78$  K, consistent with the  $T_c^{\text{zero}}$  determined from the  $\rho(T)$  data shown in the inset of Fig. 1(a). Figures 1(f) and 1(g) present the field dependences of magnetization  $M(H)$  up to 50 Oe at various temperatures from 0.39 to 0.6 K along the  $ab$  plane and the  $c$  axis, respectively. Apparently, the large magnetic hysteresis characterizes the common behavior of a type-II superconductor. A linear fitting to  $M(H)$  for the full shielding effect yields the lower critical field  $\mu_0 H_{c1}$ . Here, the obtained lower critical field values are  $H_{c1}^{\parallel ab}(0) = 9.42$  Oe and  $H_{c1}^{\parallel c}(0) = 4.7$  Oe by employing the GL formula, as displayed in Fig. 1(h). Furthermore, according to the equations  $\mu_0 H_{c1}^{\parallel c}(0) = (\Phi_0/4\pi\lambda_{ab}^2)\ln(\kappa_c)$  and  $\mu_0 H_{c1}^{\parallel ab}(0) = (\Phi_0/4\pi\lambda_{ab}\lambda_c)\ln(\kappa_{ab})$ , where the GL parameters  $\kappa_c = \lambda_{ab}/\xi_{ab}$  and  $\kappa_{ab} = \sqrt{\lambda_{ab}\lambda_c/\xi_{ab}\xi_c}$  [48], we can further estimate the penetration depth to be  $\lambda_{\text{GL}}^{ab} = 10104.8$  Å and  $\lambda_{\text{GL}}^c = 5360.9$  Å. The calculated GL parameters  $\kappa_{\text{GL}}^{ab} = 22.2$  and  $\kappa_{\text{GL}}^c = 18.5$ ,  $> 1/\sqrt{2}$ , further confirm that  $\text{RbV}_3\text{Sb}_5$  belongs to the type-II superconductors.

Figures 2(a) and 2(b) display the temperature dependences of resistivity  $\rho(T)$  and its derivative  $d\rho/dT$  at  $T < 120$  K under various pressures up to 2.2 GPa measured with a PCC and 2.4 GPa in CAC. Here, we shift the  $\rho(T)$  and  $d\rho/dT$  curves vertically for clarity. The evolution of the CDW ordering temperature with pressure can be tracked from the resistivity anomaly. At 0 GPa, the  $\rho(T)$  shows a kinklike anomaly at  $T^*$

$\approx 103$  K [Figs. 1(a) and 2(a)]. From  $d\rho/dT$ , we can actually define two characteristic temperatures, i.e.,  $T^{\text{peak}}$  and  $T^{\text{dip}}$  corresponding to the peak and dip temperatures [49,50], and determine the  $T^* = (T^{\text{peak}} + T^{\text{dip}})/2$ . Here,  $T^{\text{dip}}$  and  $T^{\text{peak}}$  are defined as the intersection point of two straight lines above and below the transition, which are correlated with the onset and the end of CDW hump. We define  $T^*$  as the average value of  $(T^{\text{dip}} + T^{\text{peak}})$  corresponding to the point where the relative change of resistivity is the strongest, aiming to emphasize the evolution of the CDW hump feature under high pressures. With increasing pressure gradually, the anomaly in  $\rho(T)$  at  $T^*$  and the corresponding  $T^{\text{peak}}$  and  $T^{\text{dip}}$  in  $d\rho/dT$  continuously move to lower temperatures. Interestingly, the width between  $T^{\text{peak}}$  and  $T^{\text{dip}}$  first shows an increase and then decreases at  $P > 1.5$  GPa. As we can see clearly, the dip feature in  $d\rho/dT$  could not be discerned at 2.4 GPa measured in CAC. Moreover, the weakening of the anomaly in resistivity has a profound influence on the superconducting transition, as we will discuss in detail below. It is noteworthy that the kink anomaly in  $\rho(T)$  at  $T^*$  changes to a humplike feature with increasing pressure [Fig. 2(a)]. A similar feature has also been observed in  $\text{CsV}_3\text{Sb}_5$  under pressure [36,41]. Due to the quasi-two-dimensional nature of the  $\text{AV}_3\text{Sb}_5$  family, it is inevitable that the interlayer interactions will be enhanced upon reducing the ionic radius of  $A$  cations. As shown in our previous work, the CDW order involves a non-vanishing order wave-vector along the  $c$  axis [36], which can explain the humplike feature in the  $\rho_c(T)$  of  $\text{RbV}_3\text{Sb}_5$  at ambient pressure [14].

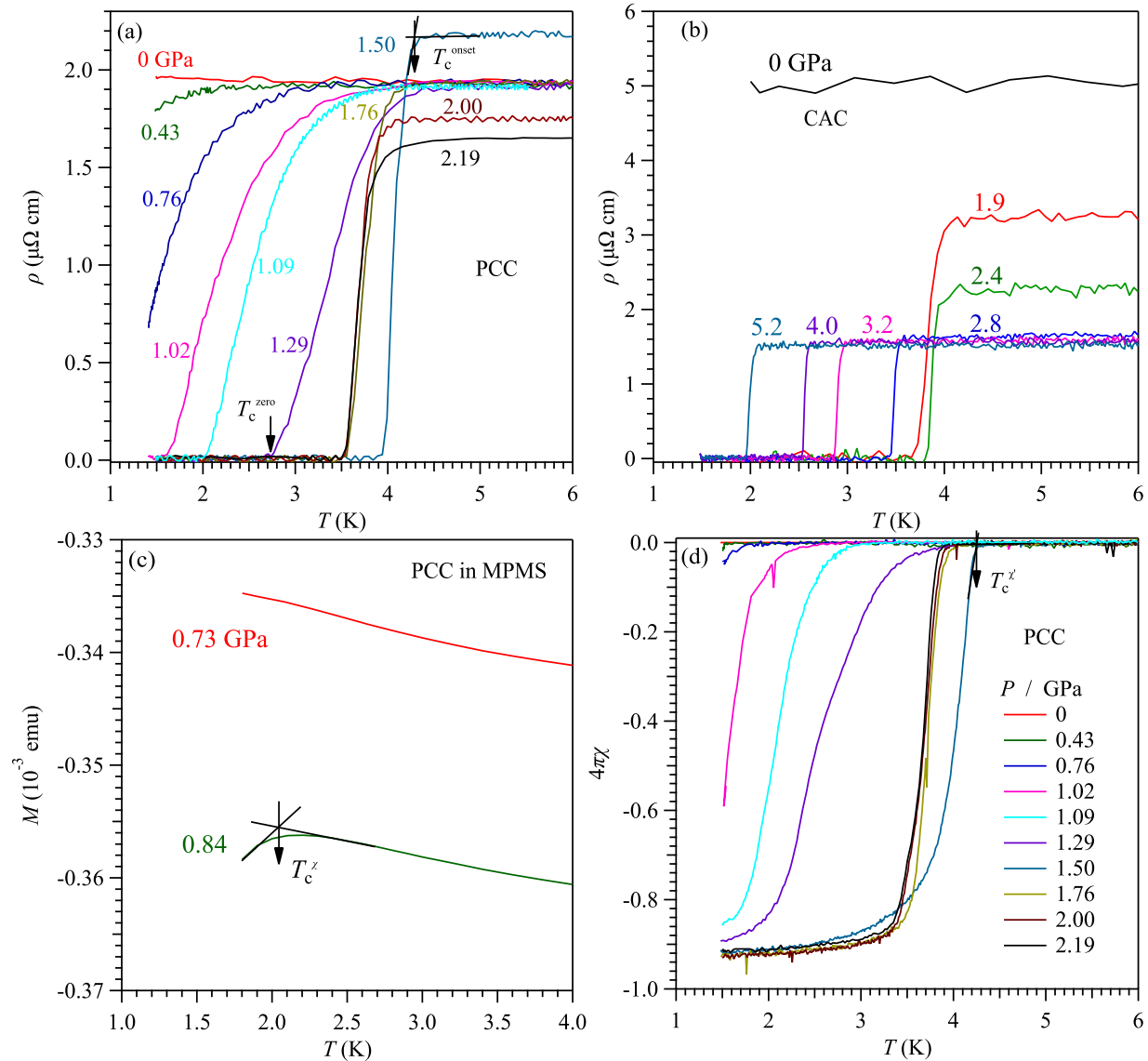


FIG. 3. Variation of the superconducting transition under high pressures in (a) and (b) resistivity and (c) and (d) magnetic susceptibility. The resistivity  $\rho(T)$  data in (a) and (b) are measured up to 2.19 GPa with a piston cylinder cell (PCC) and up to 5.2 GPa with a cubic anvil cell (CAC), respectively. The direct current (dc) magnetization in (c) was recorded in MPMS with a miniature PCC, while the alternating current (ac) magnetic susceptibility in (d) was measured with the mutual induction method in PCC.

An enlarged view of the low-temperature  $\rho(T)$  data under various pressures is present in Fig. 3(a). At ambient pressure, the superconducting transition cannot be detected down to  $T = 1.5$  K, the lowest temperature in our high-pressure measurements. When increasing pressure gradually, we start to see the weak drop of  $\rho(T)$  at 0.43 GPa and then an obvious superconducting transition at  $T_c^{\text{onset}} \approx 2.5$  K at 0.76 GPa. However, zero resistivity cannot be achieved down to 1.5 K. Here,  $T_c^{\text{onset}}$  and  $T_c^{\text{zero}}$  rapidly rise to  $\sim 3.5$  and  $\sim 1.6$  K at 1.02 GPa and then further increase to  $\sim 4$  and  $\sim 2.7$  K at 1.29 GPa, respectively. In this pressure range, the superconducting transition is broad with a transition width  $\Delta T_c > 1.5$  K. As indicated in the transition metal dichalcogenides (TMDs), some quasiskutterudite materials and synthesized kagome metals, such as  $2H\text{-Ta}(\text{S}_{1-x}\text{Se}_x)_2$  [51–53],  $\text{ZrTe}_{3-x}\text{Se}_x$  [54],  $(\text{Ca}_x\text{Sr}_{1-x})_3(\text{Rh}/\text{Ir})_4\text{Sn}_{13}$  [55,56],  $\text{KV}_3\text{Sb}_5$  [38], and  $\text{CsV}_3\text{Sb}_5$  [36,41], the competition

between CDW and SC can be tuned by doping or pressures, and we can see that the SC transition width will increase from the resistivity measurements or the superconducting volume fraction will decrease when the CDW shows strong competition with SC. Therefore, such a broad transition is consistent with the fact that SC coexists with the CDW in this regime. With increasing pressure to 1.5 GPa, the superconducting transition temperature reaches a maximum with  $T_c^{\text{onset}} \approx 4.4$  K and  $T_c^{\text{zero}} \approx 4$  K; accordingly, the superconducting transition width quickly shrinks to  $\Delta T_c \approx 0.4$  K. Interestingly, when the pressure is further increased from 1.5 to 2.19 GPa,  $T_c^{\text{onset}}$  and  $T_c^{\text{zero}}$  are reduced slightly to  $\sim 4.1$  and  $\sim 3.55$  K, respectively. In the pressure range 1.76–2.19 GPa,  $\Delta T_c$  increases slightly to  $\sim 0.6$  K. The broadened  $\Delta T_c$  highlights a complex and intrinsic phenomenon that may originate from the cryptic modification of the CDW, as discussed below.

To further track the evolution of  $T_c(P)$  under higher pressures, we measured the  $\rho(T)$  of  $\text{RbV}_3\text{Sb}_5$  up to 5.2 GPa with CAC and display the low-temperature data in Fig. 3(b). The  $\rho(T)$  in the whole temperature range are given in Fig. S3 in the Supplemental Material [57]. The  $\rho(T)$  at 0 and 1.9 GPa in CAC resembles those of 0 and 2 GPa in PCC, showing a relatively sharp superconducting transition with  $T_c^{\text{onset}} \approx 4.14$  K and  $T_c^{\text{zero}} \approx 3.66$  K at 1.9 GPa. When the pressure is gradually increased to 2.4 GPa, we can see that the normal-state resistivity shows a continuous decrease, and the  $T_c^{\text{zero}}(T_c^{\text{onset}})$  increases (decrease) slightly to  $\sim 3.8$  (3.93) K, resulting in a very sharp transition with  $\Delta T_c \approx 0.1$  K. Above 2.8 GPa, the superconducting transition shifts to lower temperatures monotonically, and the  $T_c^{\text{onset}}$  and  $T_c^{\text{zero}}$  are reduced to 2.06 and 1.96 K at 5.2 GPa. Here, we can see that the superconducting transition remains very sharp with  $\Delta T_c \approx 0.1$  K at  $P \geq 2.4$  GPa. These results indicate that the observed broadening of the superconducting transition in the intermediate pressure range is not due to the sample or pressure inhomogeneity but is an intrinsic property. These  $\rho(T)$  measurements have thus revealed a complex, nonmonotonic variation of  $T_c(P)$  in the investigated pressure range.

The evolution of the superconducting transition was further monitored by measuring the dc magnetization  $M(T)$  up to 0.84 GPa in MPMS and the ac susceptibility  $\chi'(T)$  at various pressures to 2.2 GPa in PCC. Figure 3(c) shows the ZFC  $M(T)$  data measured under an external magnetic field of  $H = 5$  Oe in the warming-up process. The diamagnetic signal in  $M(T)$  appears at  $T_c^X \approx 2$  K for 0.84 GPa, where the resistivity data show a remarkable superconducting transition. Figure 3(d) shows the  $\chi'(T)$  data at various pressures up to 2.19 GPa, and the results are in good agreement with the resistivity data shown in Fig. 3(a). Upon applying pressure gradually to 0.76 GPa, a weak diamagnetic signal can be observed at  $T < \sim 1.7$  K. At 1.02 GPa, a sharp superconducting transition in  $\chi'(T)$  can be observed with  $\sim 60\%$  superconducting volume fraction achieved at 1.5 K. With further increasing pressure, we can see a continuous increase of  $T_c^X$  from 2.86 K at 1.09 GPa to 4.29 K at 1.5 GPa, and the superconducting transition becomes much sharper at 1.5 GPa. Above 1.5 GPa, the superconducting transition was suppressed gradually, and the superconducting volume fraction reaches  $\sim 92\%$  when the CDW order nearly vanishes.

Based on the above resistivity and magnetic susceptibility measurements under high pressures, we constructed the  $T$ - $P$  phase diagram of  $\text{RbV}_3\text{Sb}_5$  as shown in Figs. 4(a) and 4(b). From the phase diagram, we can easily visualize the evolution and intertwined correlations between the CDW and SC as a function of pressure. With increasing pressure gradually, the CDW order is monotonically suppressed, accompanied by the initial enhancement of  $T_c$  with a broad superconducting transition width  $\Delta T_c \sim 2$  K for  $P < 1.5$  GPa, as displayed in Fig. 4(b) and 4(c), showing a strong competition between CDW and SC. At  $P_{c1} \approx 1.5$  GPa, the highest  $T_c^{\text{zero}} \approx 4$  K is achieved, and it is over four times higher than that at ambient pressure. Above 1.5 GPa, the resistivity anomaly associated with the CDW order becomes more weakened, while the superconducting transition temperature shows a shallow valley between 1.5 and 2.4 GPa. It seems that the long-range CDW order has been replaced by a short-ranged one that

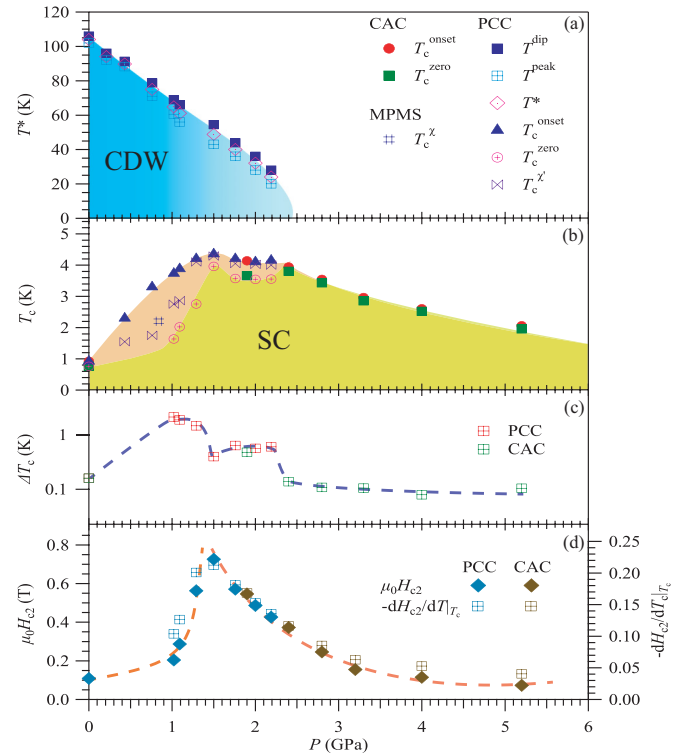


FIG. 4. Temperature-pressure phase diagram of  $\text{RbV}_3\text{Sb}_5$ . Pressure dependences of (a)  $T^*$ , (b)  $T_c$ , and (c) the superconducting transition width  $\Delta T_c$  determined from the resistivity and magnetic measurements on several samples, and (d) left shows the zero-temperature upper critical field  $\mu_0 H_{c2}(0)$  obtained from the empirical Ginzburg-Landau (GL) fitting, and right shows the initial slope of upper critical field  $\mu_0 H_{c2}$  determined from the linear fitting to the data in Figs. 5(a) and 5(b).

coexists with SC in this pressure range and thus leads to a broadening of the superconducting transition, Figs. 4(b) and 4(c). Compared with the widely studied TMDs, the long-range CDW order can be gradually suppressed by doping or high pressure, leaving the short-ranged CDW fluctuations to dominate the transport behavior [52,54,58,59]. Accordingly, the density of states at the Fermi level changes very little, and the CDW-induced hump is gradually diminished [58]. Once the long-range CDW phase coherence was influenced, the broadened superconducting transition and slightly reduced  $T_c$  was exhibited in the resistivity. As is shown in Fig. 2(a), the CDW-related hump can be seen clearly in resistivity with noticeable dip and peak features on its derivative at  $P < 1.5$  GPa. When the pressure gradually increases to 2.19 GPa, we can see that the CDW anomaly in resistivity is gradually smeared out, and the dip and peak features are gradually weakened and broadened, accompanying a slightly reduced  $T_c$  and broadened SC transition. Therefore, we assume that the long-range CDW order transforms to short-ranged CDW order due to the differences in resistivity and its derivative below and above 1.5 GPa. The complete suppression of the short-ranged CDW order gives the second maximum of  $T_c^{\text{zero}}$  around  $P_{c2} \approx 2.4$  GPa. Above 2.4 GPa, the superconducting transition monotonically moves to lower temperatures and becomes very sharp with  $\Delta T_c \approx 0.1$  K, Fig. 4(c).

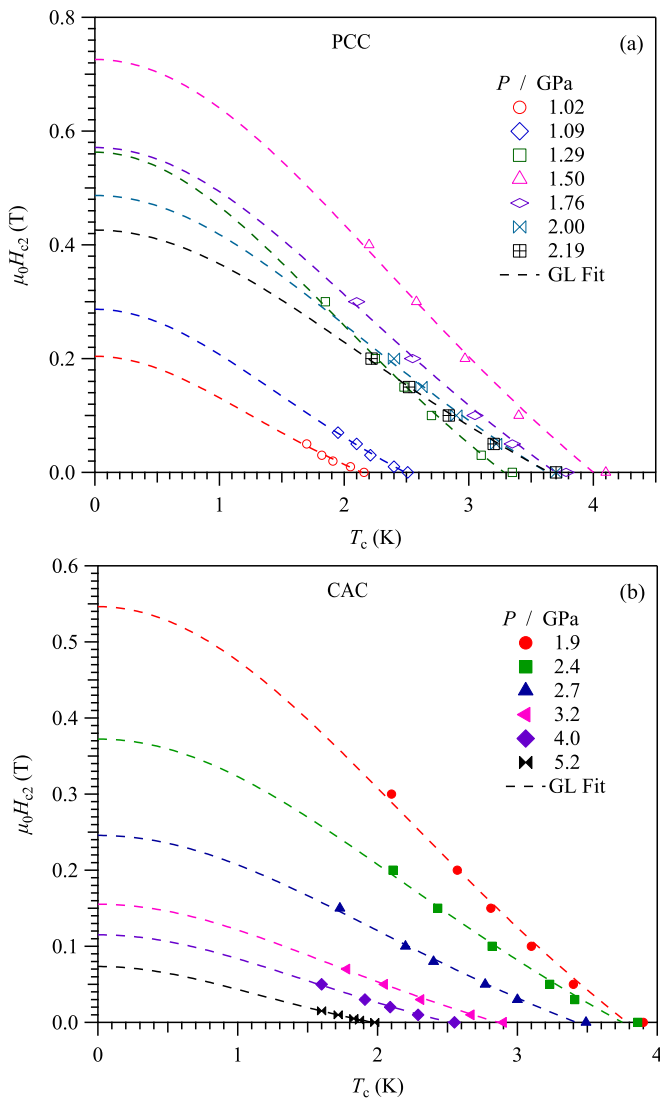


FIG. 5. Temperature dependences of the upper critical field  $\mu_0 H_{c2}$  at different pressures measured with (a) a piston cylinder cell (PCC) and (b) a cubic anvil cell (CAC). The broken lines represent the Ginzburg-Landau (GL) fitting curves.

To further probe the evolution of the superconducting electronic states of  $\text{RbV}_3\text{Sb}_5$  under high pressures, we measured the upper critical field  $\mu_0 H_{c2}$  at various pressures up to 5.2 GPa. All  $\rho(T)$  data under various magnetic fields and different pressures in PCC and CAC are shown in Fig. S4 in the Supplemental Material [57]. Here,  $T_c$  moves to lower temperatures gradually with increasing magnetic fields. To track the evolution of  $\mu_0 H_{c2}$ , we employed the criteria of middle-point temperature  $T_c^{\text{mid}}$  as the superconducting transition temperature. As shown in Fig. 5, we plot all  $\mu_0 H_{c2}(T)$  data measured in PCC and CAC and then estimate the zero-temperature  $\mu_0 H_{c2}(0)$  by employing the empirical GL equation, as discussed above, to fit the  $\mu_0 H_{c2}(T)$  data. The best fitting results are indicated by the broken lines in Figs. 5(a) and 5(b). Surprisingly, the  $\mu_0 H_{c2}(0)$  as a function of pressure exhibits a pronounced peak around  $P_{c1} \approx 1.5$  GPa [Fig. 4(d)] but not at  $P_{c2}$ . This result is different from the double peak feature observed in  $\text{CsV}_3\text{Sb}_5$  [36,41]. We also extract the initial slope

of  $\mu_0 H_{c2}(T)$  at each pressure, i.e.,  $-dH_{c2}/dT|_{T_c}$ , and a similar peak feature shows around  $P_{c1}$ , Fig. 4(d). As the slope  $-dH_{c2}/dT|_{T_c}$  is proportional to the effective mass of charge carriers [60], the divergence of  $-dH_{c2}/dT|_{T_c}$  around  $P_{c1} \approx 1.5$  GPa indicates an enhancement of effective mass, as shown in Fig. 4(d). In general, the divergence of effective mass is considered a hallmark of quantum criticality due to a complete suppression of certain electronic order [9,61]. It should be noted that the optimal superconducting phase usually emerges at the quantum critical point (QCP) in many unconventional superconductors [62–66].

#### IV. DISCUSSIONS

By combining resistivity and magnetic susceptibility measurements, we have tracked the evolutions of the CDW order and SC in  $\text{RbV}_3\text{Sb}_5$  and unveiled a shallow M-shaped double superconducting dome under pressure, as described above. With increasing pressure,  $T^*(P)$  decreases monotonically and vanishes completely around  $P_{c2} \approx 2.4$  GPa, while  $T_c(P)$  exhibits two maxima at  $P_{c1} \approx 1.5$  GPa and  $P_{c2}$ , respectively. Above  $P_{c2}$ , the CDW order is eliminated, and the superconducting transition shows a monotonic reduction. The highest  $T_c^{\text{onset}} \approx 4.4$  K is achieved around  $P_{c1} \approx 1.5$  GPa rather than the putative QCP of the CDW order located at  $P_{c2} \approx 2.4$  GPa. The optimal  $T_c^{\text{onset}} \approx 4.4$  K around  $P_{c1}$  is about fourfold enhanced in comparison with that at ambient pressure. All these characteristics in the  $T$ - $P$  phase diagram of  $\text{RbV}_3\text{Sb}_5$  are like those of the sister compound  $\text{CsV}_3\text{Sb}_5$  [36] but with some quantitative differences between them. In addition, their double superconducting domes are also distinct from the observed single dome in  $\text{KV}_3\text{Sb}_5$  under pressure [38]. Thus, side-by-side comparisons among them are merited to have a better understanding of the unique properties of the  $\text{AV}_3\text{Sb}_5$  family.

First, the character of the superconducting dome seems to correlate intimately with the  $A$ -cation size or the interlayer distance; the double-dome feature is weakened and changed to a single dome upon reducing the  $A$ -cation size from Cs through Rb to K. For  $\text{CsV}_3\text{Sb}_5$ , the larger Cs ion or interlayer distance should reduce the interlayer hopping and make the bands less dispersive along the  $c$  axis. In principle, the highly two-dimensional character favors the formation of the CDW order through the nesting scattering between van Hove points. Under high pressures, the bands become more dispersive along the  $c$  axis with reducing the interlayer distance and thus weaken the nesting scattering effect. The modification or vanishing of this out-of-plane CDW wave vector along the  $c$  axis under pressure would give rise to the first SC dome around  $P_{c1}$ . In comparison with  $\text{CsV}_3\text{Sb}_5$ , the interlayer distance has been compressed chemically in  $\text{RbV}_3\text{Sb}_5$ , and thus, the modification of the CDW component along the  $c$  axis is expected to be weakened, which would lead to a shallow M-shaped superconducting phase. Meanwhile, for  $\text{KV}_3\text{Sb}_5$  with much smaller interlayer distance, the bands along the  $c$  axis become more dispersive, and therefore, the double-dome character becomes much more weakened or even vanishes, as observed.

Secondly, although  $T^*(P)$  displays monotonic suppression under physical pressure for these three compounds, the evolution of  $T^*$  does not exhibit a similar trend as a function

of A-cation size; it is peaked out at  $\text{RbV}_3\text{Sb}_5$  with  $T^* = 104$  K in comparison with that of 94 K for  $\text{CsV}_3\text{Sb}_5$  and 78 K for  $\text{KV}_3\text{Sb}_5$ , respectively [12–14], while in the reported results, the observed exact zero-resistivity superconducting transition occurs at  $T_c \sim 0.93, 0.78,$  and  $2.5$  K for  $\text{KV}_3\text{Sb}_5, \text{RbV}_3\text{Sb}_5,$  and  $\text{CsV}_3\text{Sb}_5$ , as revealed by resistivity, magnetization, and specific heat [12–14]. Therefore, when compared with  $\text{RbV}_3\text{Sb}_5$ ,  $\text{KV}_3\text{Sb}_5$  has a lower  $T^* \sim 78$  K and higher  $T_c \sim 0.93$  K, and  $\text{CsV}_3\text{Sb}_5$  also has a lower  $T^* \sim 94$  K and higher  $T_c \sim 2.5$  K. Accordingly, the superconducting  $T_c$  at ambient pressure exhibits exactly the opposite trend when compared with  $\text{RbV}_3\text{Sb}_5$ , illustrating a competition nature between these two intertwined orders. These comparisons highlight that the physical and chemical pressures should play some distinct roles in modifying the crystal and electronic structures that may need further investigations. Nonetheless, the critical pressures for the suppression of the CDW order have a positive correlation with  $T^*$  at ambient pressure, i.e., the corresponding critical pressures are decreased gradually from  $P_{c1} \approx 1.5$  GPa and  $P_{c2} \approx 2.4$  GPa for  $\text{RbV}_3\text{Sb}_5$ , to  $P_{c1} \approx 0.6\text{--}0.9$  GPa and  $P_{c2} \approx 2$  GPa for  $\text{CsV}_3\text{Sb}_5$  [36], and finally to  $P_{c1} \approx 0.4\text{--}0.5$  GPa for  $\text{KV}_3\text{Sb}_5$  [38].

Thirdly, the most interesting differences between  $\text{CsV}_3\text{Sb}_5$  and  $\text{RbV}_3\text{Sb}_5$  under pressure are the distinct behaviors of  $\mu_0 H_{c2}(P)$  and its connection with the optimal  $T_c$ . For the former, the  $\mu_0 H_{c2}(0)$  shows two peaks at  $P_{c1}$  and  $P_{c2}$ , and the maximum  $T_c$  emerges at  $P_{c2}$ , accompanying the complete suppression of the CDW order; however, for the latter, both the  $\mu_0 H_{c2}(0)$  and  $T_c$  are peaked out at  $P_{c1}$  rather than  $P_{c2}$ . Then the question naturally arises why the maximal  $\mu_0 H_{c2}(0)$  and  $T_c$  in  $\text{RbV}_3\text{Sb}_5$  do not show up at  $P_{c2}$ , which is expected to possess the strongest CDW fluctuations. Although more experiments are needed to clarify this issue, some hints from the experiments are noteworthy. That is, the observed shallower valley of the double superconducting dome in  $\text{RbV}_3\text{Sb}_5$  indicates that the competition between CDW and SC in the intermediate pressure range 1.5–2.4 GPa is more weakened in comparison with  $\text{CsV}_3\text{Sb}_5$ . As a result, the CDW fluctuations around  $P_{c2}$  do not contribute significantly to the enhancement of  $T_c$  as well as the electronic correlations.

Finally, it is noteworthy that the unusual double-dome superconducting phase observed in  $\text{CsV}_3\text{Sb}_5$  and  $\text{RbV}_3\text{Sb}_5$  is reminiscent of the phase diagrams of high-temperature cuprates [64,67,68] and FeSe-based superconductors [65], showing the presence of competing intertwined CDW/SDW or nematic orders. As indicated from the theoretical calculations [28,29,32], multiple electronic orders can be achieved as a function of onsite repulsion  $U$  and nearest-neighbor Coulomb interaction  $V$ , such as ferromagnetism, intra-unit-cell antiferromagnetism, charge bond order, or spin bond order. Thus, more experiments such as high-pressure nuclear magnetic resonance should be performed to further investigate the evolution of microscopic electronic orders in these V-based kagome metals.

## V. CONCLUSIONS

In summary, we have performed a comprehensive high-pressure study on  $\text{RbV}_3\text{Sb}_5$  single crystals by employing electrical transport and magnetic susceptibility measurements. At ambient pressure, the kagome metal  $\text{RbV}_3\text{Sb}_5$  shows a charge order or CDW-like order at  $T^* = 103$  K and SC at  $T_c^{\text{zero}} = 0.78$  K. Our results reveal a subtle modification of the CDW order around  $P_{c1} \approx 1.5$  GPa, and the modified CDW is completely suppressed at  $P_{c2} \approx 2.4$  GPa. Correspondingly, the superconducting  $T_c(P)$  displays the unusual M-shaped double superconducting dome structure with the optimal  $T_c^{\text{onset}} \approx 4.4$  K and  $T_c^{\text{zero}} \approx 4$  K at 1.5 GPa and another maximum  $T_c^{\text{onset}} \approx 3.93$  K and  $T_c^{\text{zero}} \approx 3.8$  K occurring at 2.4 GPa. Therefore, our phase diagram reveals the intimate interplay and strong competition between the CDW and SC in the pressure range  $0 \text{ GPa} \leq P \leq 1.5 \text{ GPa}$ , as evidenced by the broad superconducting transition width. Between 1.5 and 2.4 GPa, the superconducting phase shows a valley character with possible underlying modification of the CDW. In addition, the  $\mu_0 H_{c2}(0)$  shows a prominent peak character at  $P_{c1} \sim 1.5$  GPa, showing the characteristics of quantum criticality associated with the suppression of CDW order. The constructed  $T$ - $P$  phase diagram is like those of many unconventional superconductors with intertwined electronic orders. Therefore,  $\text{RbV}_3\text{Sb}_5$  together with  $\text{CsV}_3\text{Sb}_5$  provides a platform to study the correlations between the electronic instabilities and SC in this topological kagome metal family. In addition, the optimal  $T_c$  of  $\text{RbV}_3\text{Sb}_5$  reaches  $\sim 4.4$  K at 1.5 GPa, which gives the possibility to further enhance  $T_c$  of these V-based kagome superconductors. Further studies on  $\text{RbV}_3\text{Sb}_5$  are needed to address the open issues such as the character of the CDW-like order in the intermediate pressure range.

## ACKNOWLEDGMENTS

This paper is supported by the National Natural Science Foundation of China (Grants No. 12025408, No. 11904391, No. 11921004, No. 11888101, No. 11834016, No. 11822412, and No. 11774423), the Beijing Natural Science Foundation (Grants No. Z190008 and No. Z200005), the National Key R&D Program of China (Grants No. 2018YFA0305700, No. 2018YFE0202600, and No. 2016YFA0300504), the Strategic Priority Research Program and Key Research Program of Frontier Sciences of the Chinese Academy of Sciences (Grants No. XDB25000000, No. XDB33000000, and No. QYZDB-SSW-SLH013), the CAS Interdisciplinary Innovation Team, the Excellence Program of Hefei Science Center CAS (Grant No. 2021HSC-UE008), the Fundamental Research Funds for the Central Universities and Research Funds of Renmin University of China (Grants No. 18XNLG14 and No. 19XNLG17), and the Beijing National Laboratory for Condensed Matter Physics. U.W. is supported by the JSPS KAKENHI Grant No. 19H00648.

[1] J. C. Phillips, A. Saxena, and A. R. Bishop, Pseudogaps, dopants, and strong disorder in cuprate high-temperature superconductors, *Rep. Prog. Phys.* **66**, 2111 (2003).

[2] N. P. Armitage, P. Fournier, and R. L. Greene, Progress and perspectives on electron-doped cuprates, *Rev. Mod. Phys.* **82**, 2421 (2010).



- [3] E. Dagotto, The unexpected properties of alkali metal iron selenide superconductors, *Rev. Mod. Phys.* **85**, 849 (2013).
- [4] E. Fradkin, S. A. Kivelson, and J. M. Tranquada, Theory of intertwined orders in high temperature superconductors, *Rev. Mod. Phys.* **87**, 457 (2015).
- [5] I. I. Mazin, Superconductivity gets an iron boost, *Nature (London)* **464**, 183 (2010).
- [6] J. Paglione and R. L. Greene, High-temperature superconductivity in iron-based materials, *Nat. Phys.* **6**, 645 (2010).
- [7] Q. Si, R. Yu, and E. Abrahams, High-temperature superconductivity in iron pnictides and chalcogenides, *Nat. Rev. Materials* **1**, 16017 (2016).
- [8] G. R. Stewart, Superconductivity in iron compounds, *Rev. Mod. Phys.* **83**, 1589 (2011).
- [9] Z. F. Weng, M. Smidman, L. Jiao, X. Lu, and H. Q. Yuan, Multiple quantum phase transitions and superconductivity in Ce-based heavy fermions, *Rep. Prog. Phys.* **79**, 094503 (2016).
- [10] S. Wirth and F. Steglich, Exploring heavy fermions from macroscopic to microscopic length scales, *Nat. Rev. Materials* **1**, 16051 (2016).
- [11] B. R. Ortiz, L. C. Gomes, J. R. Morey, M. Winiarski, M. Bordelon, J. S. Mangum, I. W. H. Oswald, J. A. Rodriguez-Rivera, J. R. Neilson, S. D. Wilson, E. Ertekin, T. M. McQueen, and E. S. Toberer, New kagome prototype materials: discovery of  $KV_3Sb_5$ ,  $RbV_3Sb_5$ , and  $CsV_3Sb_5$ , *Phys. Rev. Mater.* **3**, 094407 (2019).
- [12] B. R. Ortiz, S. M. L. Teicher, Y. Hu, J. L. Zuo, P. M. Sarte, E. C. Schueller, A. M. M. Abeykoon, M. J. Krogstad, S. Rosenkranz, R. Osborn, R. Seshadri, L. Balents, J. He, and S. D. Wilson,  $CsV_3Sb_5$ : A  $Z_2$  Topological Kagome Metal with a Superconducting Ground State, *Phys. Rev. Lett.* **125**, 247002 (2020).
- [13] B. R. Ortiz, E. Kenney, P. M. Sarte, S. M. L. Teicher, R. Seshadri, M. J. Graf, and S. D. Wilson, Superconductivity in the  $Z_2$  kagome metal  $KV_3Sb_5$ , *Phys. Rev. Materials* **5**, 034801 (2021).
- [14] Q. W. Yin, Z. J. Tu, C. S. Gong, Y. Fu, S. H. Yan, and H. C. Lei, Superconductivity and normal-state properties of kagome metal  $RbV_3Sb_5$  single crystals, *Chin. Phys. Lett.* **38**, 037403 (2021).
- [15] Y. X. Jiang, J. X. Yin, M. M. Denner, N. Shumiya, B. R. Ortiz, G. Xu, Z. Guguchia, J. Y. He, M. S. Hossain, X. X. Liu, J. Ruff, L. Kautzsch, S. S. Zhang, G. Q. Chang, I. Belopolski, Q. Zhang, T. A. Cochran, D. Multer, M. Litskevich, Z. J. Cheng *et al.*, Unconventional chiral charge order in kagome superconductor  $KV_3Sb_5$ , *Nat. Mater.* **20**, 1353 (2021).
- [16] H. Chen, H. Yang, B. Hu, Z. Zhao, J. Yuan, Y. Xing, G. Qian, Z. Huang, G. Li, Y. Ye, S. Ma, S. Ni, H. Zhang, Q. Yin, C. Gong, Z. Tu, H. Lei, H. Tan, S. Zhou, C. Shen, X. Dong, B. Yan *et al.*, Roton pair density wave in a strong-coupling kagome superconductor, *Nature* (2021), doi:10.1038/s41586-021-03983-5.
- [17] H. Li, H. Zhao, B. R. Ortiz, T. Park, M. X. Ye, L. Balents, Z. Q. Wang, S. D. Wilson, and I. Zeljkovic, Rotation symmetry breaking in the normal state of a kagome superconductor  $KV_3Sb_5$ , *arXiv:2104.08209* (2021).
- [18] H. Li, T. T. Zhang, T. Yilmaz, Y. Y. Pai, C. E. Marvinney, A. Said, Q. W. Yin, C. S. Gong, Z. J. Tu, E. Vescovo, C. S. Nelson, R. G. Moore, S. Murakami, H. C. Lei, H. N. Lee, B. J. Lawrie, and H. Miao, Observation of Unconventional Charge Density Wave without Acoustic Phonon Anomaly in Kagome Superconductors  $AV_3Sb_5$  ( $A = Rb, Cs$ ), *Phys. Rev. X* **11**, 031050 (2021).
- [19] Z. W. Liang, X. Y. Hou, W. R. Ma, F. Zhang, P. Wu, Z. Y. Zhang, F. H. Yu, J. J. Ying, K. Jiang, L. Shan, Z. Y. Wang, and X. H. Chen, Three-Dimensional Charge Density Wave and Robust Zero-Bias Conductance Peak Inside the Superconducting Vortex Core of a Kagome Superconductor  $CsV_3Sb_5$ , *Phys. Rev. X* **11**, 031026 (2021).
- [20] B. R. Ortiz, S. M. L. Teicher, L. Kautzsch, P. M. Sarte, J. P. C. Ruff, R. Seshadri, and S. D. Wilson, Fermi surface mapping and the nature of charge density wave order in the kagome superconductor  $CsV_3Sb_5$ , *arXiv:2104.07230* (2021).
- [21] N. Ratchiff, L. Hallett, B. R. Ortiz, S. D. Wilson, and J. W. Harter, Coherent phonon spectroscopy and inter layer modulation of charge density wave order in the kagome metal  $CsV_3Sb_5$ , *arXiv:2104.10138* (2021).
- [22] E. Uykur, B. R. Ortiz, O. Iakutkina, M. Wenzel, S. D. Wilson, M. Dressel, and A. A. Tsirlin, Low-energy optical properties of the non-magnetic kagome metal  $CsV_3Sb_5$ , *Phys. Rev. B* **104**, 045130 (2021).
- [23] H. Zhao, H. Li, B. R. Ortiz, S. M. L. Teicher, T. Park, M. X. Ye, Z. Q. Wang, L. Balents, S. D. Wilson, and I. Zeljkovic, Cascade of correlated electron states in a kagome superconductor  $CsV_3Sb_5$ , *Nature* (2021), doi:10.1038/s41586-021-03946-w.
- [24] X. X. Zhou, Y. K. Li, X. W. Fan, J. H. Hao, Y. M. Dai, Z. W. Wang, Y. G. Yao, and H. H. Wen, Origin of the Charge Density Wave in the Kagome Metal  $CsV_3Sb_5$  as Revealed by Optical Spectroscopy, *Phys. Rev. B* **104**, L041101 (2021).
- [25] X. L. Feng, K. Jiang, Z. Q. Wang, and J. P. Hu, Chiral flux phase in the kagome superconductor  $AV_3Sb_5$ , *Sci. Bull.* **66**, 1384 (2021).
- [26] A. O'Brien, F. Pollmann, and P. Fulde, Strongly correlated fermions on a kagome lattice, *Phys. Rev. B* **81**, 235115 (2010).
- [27] S. V. Isakov, S. Wessel, R. G. Melko, K. Sengupta, and Y. B. Kim, Hard-Core Bosons on the Kagome Lattice: Valence-Bond Solids and Their Quantum Melting, *Phys. Rev. Lett.* **97**, 147202 (2006).
- [28] M. L. Kiesel, C. Platt, and R. Thomale, Unconventional Fermi Surface Instabilities in the Kagome Hubbard Model, *Phys. Rev. Lett.* **110**, 126405 (2013).
- [29] W. S. Wang, Z. Z. Li, Y. Y. Xiang, and Q. H. Wang, Competing electronic orders on kagome lattices at van Hove filling, *Phys. Rev. B* **87**, 115135 (2013).
- [30] M. M. Denner, R. Thomale, and T. Neupert, Analysis of charge order in the kagome metal  $AV_3Sb_5$  ( $A = K, Rb, Cs$ ), *arXiv:2103.14045* (2021).
- [31] Y. P. Lin and R. M. Nandkishore, Complex charge density waves at Van Hove singularity on hexagonal lattices: haldane-model phase diagram and potential realization in kagome metals  $AV_3Sb_5$ , *Phys. Rev. B* **104**, 045122 (2021).
- [32] S. L. Yu and J. X. Li, Chiral superconducting phase and chiral spin-density-wave phase in a Hubbard model on the kagome lattice, *Phys. Rev. B* **85**, 144402 (2012).
- [33] W. H. Ko, P. A. Lee, and X. G. Wen, Doped kagome system as exotic superconductor, *Phys. Rev. B* **79**, 214502 (2009).
- [34] M. L. Kiesel and R. Thomale, Sublattice interference in the kagome Hubbard model, *Phys. Rev. B* **86**, 121105(R) (2012).
- [35] A. Rüegg and G. A. Fiete, Fractionally charged topological point defects on the kagome lattice, *Phys. Rev. B* **83**, 165118 (2011).

- [36] K. Y. Chen, N. N. Wang, Q. W. Yin, Y. H. Gu, K. Jiang, Z. J. Tu, C. S. Gong, Y. Uwatoko, J. P. Sun, H. C. Lei, J. P. Hu, and J. G. Cheng, Double Superconducting Dome and Triple Enhancement of  $T_c$  in the Kagome Superconductor  $\text{CsV}_3\text{Sb}_5$  Under High Pressure, *Phys. Rev. Lett.* **126**, 247001 (2021).
- [37] X. Chen, X. H. Zhan, X. J. Wang, J. Deng, X. B. Liu, X. Chen, J. G. Guo, and X. L. Chen, Highly-robust reentrant superconductivity in  $\text{CsV}_3\text{Sb}_5$  under pressure, *Chin. Phys. Lett.* **38**, 057402 (2021).
- [38] F. Du, S. S. Luo, B. R. Ortiz, Y. Chen, W. Y. Duan, D. T. Zhang, X. Lu, S. D. Wilson, Y. Song, and H. Q. Yuan, Pressure-induced double superconducting domes and charge instability in the kagome metal  $\text{KV}_3\text{Sb}_5$ , *Phys. Rev. B* **103**, L220504 (2021).
- [39] Z. Y. Zhang, Z. Chen, Y. Zhou, Y. F. Yuan, S. Y. Wang, J. Wang, H. Y. Yang, C. An, L. L. Zhang, X. D. Zhu, Y. H. Zhou, X. L. Chen, J. H. Zhou, and Z. R. Yang, Pressure-induced reemergence of superconductivity in topological kagome metal  $\text{CsV}_3\text{Sb}_5$ , *Phys. Rev. B* **103**, 224513 (2021).
- [40] C. C. Zhao, L. S. Wang, W. Xia, Q. W. Yin, J. M. Ni, Y. Y. Huang, C. P. Tu, Z. C. Tao, Z. J. Tu, C. S. Gong, H. C. Lei, Y. F. Guo, X. F. Yang, and S. Y. Li, Nodal superconductivity and superconducting dome in the topological Kagome metal  $\text{CsV}_3\text{Sb}_5$ , [arXiv:2102.08356](https://arxiv.org/abs/2102.08356) (2021).
- [41] F. H. Yu, D. H. Ma, W. Z. Zhuo, S. Q. Liu, X. K. Wen, B. Lei, J. J. Ying, and X. H. Chen, Unusual competition of superconductivity and charge-density-wave state in a compressed topological kagome metal, *Nat. Commun.* **12**, 3645 (2021).
- [42] H. X. Tan, Y. Z. Liu, Z. Q. Wang, and B. H. Yan, Charge Density Waves and Electronic Properties of Superconducting Kagome Metals, *Phys. Rev. Lett.* **127**, 046401 (2021).
- [43] C. C. Zhu, X. F. Yang, W. Xia, Q. W. Yin, L. S. Wang, C. C. Zhao, D. Z. Dai, C. P. Tu, B. Q. Song, Z. C. Tao, Z. J. Tu, C. S. Gong, H. C. Lei, Y. F. Guo, and S. Y. Li, Double-dome superconductivity under pressure in the V-based kagome metals  $\text{AV}_3\text{Sb}_5$  ( $A = \text{Rb}$  and  $\text{K}$ ), [arXiv:2104.14487](https://arxiv.org/abs/2104.14487) (2021).
- [44] Y. Uwatoko, S. Todo, K. Ueda, A. Uchida, M. Kosaka, N. Mori, and T. Matsumoto, Material properties of Ni-Cr-Al alloy and design of a 4 GPa class non-magnetic high-pressure cell, *J. Phys.: Condens. Matter* **14**, 11291 (2002).
- [45] J. G. Cheng, K. Matsubayashi, S. Nagasaki, A. Hisada, T. Hirayama, M. Hedo, H. Kagi, and Y. Uwatoko, Integrated-fin gasket for palm cubic-anvil high pressure apparatus, *Rev. Sci. Instrum.* **85**, 093907 (2014).
- [46] S. I. Vedenev, B. A. Piot, D. K. Maude, and A. V. Sadakov, Temperature dependence of the upper critical field of FeSe single crystals, *Phys. Rev. B* **87**, 134512 (2013).
- [47] S. L. Ni, S. Ma, Y. H. Zhang, J. Yuan, H. T. Yang, Z. Y. W. Lu, N. N. Wang, J. P. Sun, Z. Zhao, D. Li, S. B. Liu, H. Zhang, H. Chen, K. Jin, J. G. Cheng, L. Yu, F. Zhou, X. L. Dong, J. P. Hu, H. J. Gao *et al.*, Anisotropic superconducting properties of kagome metal  $\text{CsV}_3\text{Sb}_5$ , *Chin. Phys. Lett.* **38**, 057403 (2021).
- [48] Y. J. Song, J. S. Ghim, J. H. Yoon, K. J. Lee, M. H. Jung, H. S. Ji, J. H. Shim, Y. Bang, and Y. S. Kwon, Small anisotropy of the lower critical field and the  $s_{\pm}$ -wave two-gap feature in single-crystal  $\text{LiFeAs}$ , *EPL* **94**, 57008 (2011).
- [49] J. J. Hamlin, D. A. Zocco, T. A. Sayles, M. B. Maple, J. H. Chu, and I. R. Fisher, Pressure-Induced Superconducting Phase in the Charge-Density-Wave Compound Terbium Tritelluride, *Phys. Rev. Lett.* **102**, 177002 (2009).
- [50] K. Cho, M. Konczykowski, S. Teknowijoyo, M. A. Tanatar, J. Guss, P. B. Gartin, J. M. Wilde, A. Kreyssig, R. J. McQueeney, A. I. Goldman, V. Mishra, P. J. Hirschfeld, and R. Prozorov, Using controlled disorder to probe the interplay between charge order and superconductivity in  $\text{NbSe}_2$ , *Nat. Commun.* **9**, 2796 (2018).
- [51] D. C. Freitas, P. Rodière, M. R. Osorio, E. Navarro-Moratalla, N. M. Nemes, V. G. Tissen, L. Cario, E. Coronado, M. García-Hernández, S. Vieira, M. Núñez-Regueiro, and H. Suderow, Strong enhancement of superconductivity at high pressures within the charge-density-wave states of  $2H$ - $\text{TaS}_2$  and  $2H$ - $\text{TaSe}_2$ , *Phys. Rev. B* **93**, 184512 (2016).
- [52] L. J. Li, X. Y. Deng, Z. Wang, Y. Liu, M. Abeykoon, E. Dooryhee, A. Tomic, Y. N. Huang, J. B. Warren, E. S. Bozin, S. J. L. Billinge, Y. P. Sun, Y. M. Zhu, G. Kotliar, and C. Petrovic, Superconducting order from disorder in  $2H$ - $\text{TaSe}_{2-x}\text{S}_x$ , *npj Quantum Materials* **2**, 11 (2017).
- [53] S. X. Xu, Z. Y. Liu, P. T. Yang, K. Y. Chen, J. P. Sun, J. H. Dai, Y. Y. Yin, F. Hong, X. H. Yu, M. Q. Xue, J. Gouchi, Y. Uwatoko, B. S. Wang, and J. G. Cheng, Superconducting phase diagrams of S-doped  $2H$ - $\text{TaSe}_2$  under hydrostatic pressure, *Phys. Rev. B* **102**, 184511 (2020).
- [54] X. Zhu, W. Ning, L. Li, L. Ling, R. Zhang, J. Zhang, K. Wang, Y. Liu, L. Pi, Y. Ma, H. Du, M. Tian, Y. Sun, C. Petrovic, and Y. Zhang, Superconductivity and Charge Density Wave in  $\text{ZrTe}_{3-x}\text{Se}_x$ , *Sci. Rep.* **6**, 26974 (2016).
- [55] L. E. Klintberg, S. K. Goh, P. L. Alireza, P. J. Saines, D. A. Tompsett, P. W. Logg, J. Yang, B. Chen, K. Yoshimura, and F. M. Grosche, Pressure- and Composition-Induced Structural Quantum Phase Transition in the Cubic Superconductor  $(\text{Sr}, \text{Ca})_3\text{Ir}_4\text{Sn}_{13}$ , *Phys. Rev. Lett.* **109**, 237008 (2012).
- [56] S. K. Goh, D. A. Tompsett, P. J. Saines, H. C. Chang, T. Matsumoto, M. Imai, K. Yoshimura, and F. M. Grosche, Ambient Pressure Structural Quantum Critical Point in the Phase Diagram of  $(\text{Ca}_x\text{Sr}_{1-x})_3\text{Rh}_4\text{Sn}_{13}$ , *Phys. Rev. Lett.* **114**, 097002 (2015).
- [57] See Supplemental Material at <http://link.aps.org/supplemental/10.1103/PhysRevResearch.3.043018> for sample characterization and high pressure resistivity.
- [58] A. Taraphder, S. Koley, N. S. Vidhyadhiraja, and M. S. Laad, Preformed Excitonic Liquid Route to a Charge Density Wave in  $2H$ - $\text{TaSe}_2$ , *Phys. Rev. Lett.* **106**, 236405 (2011).
- [59] J. Joshi, H. M. Hill, S. Chowdhury, C. D. Malliakas, F. Tavazza, U. Chatterjee, A. R. Hight Walker, and P. M. Vora, Short-range charge density wave order in  $2H$ - $\text{TaS}_2$ , *Phys. Rev. B* **99**, 245144 (2019).
- [60] V. G. Kogan and R. Prozorov, Orbital upper critical field and its anisotropy of clean one- and two-band superconductors, *Rep. Prog. Phys.* **75**, 114502 (2012).
- [61] J. Zaanen, Quantum critical electron systems: the uncharted sign worlds, *Science* **319**, 1205 (2008).
- [62] Y. Nakajima, H. Shishido, H. Nakai, T. Shibauchi, K. Behnia, K. Izawa, M. Hedo, Y. Uwatoko, T. Matsumoto, R. Settai, Y. Ōnuki, H. Kontani, and Y. Matsuda, Non-Fermi liquid behavior in the magnetotransport of  $\text{CeMIn}_5$  ( $M$ : Co and Rh): striking similarity between quasi two-dimensional heavy fermion and high- $T_c$  cuprates, *J. Phys. Soc. Jpn.* **76**, 024703 (2007).
- [63] J. C. Davis and D. H. Lee, Concepts relating magnetic interactions, intertwined electronic orders, and strongly correlated

- superconductivity, *Proc. Natl. Acad. Sci. USA* **110**, 17623 (2013).
- [64] B. Keimer, S. A. Kivelson, M. R. Norman, S. Uchida, and J. Zaanen, From quantum matter to high-temperature superconductivity in copper oxides, *Nature (London)* **518**, 179 (2015).
- [65] J. P. Sun, K. Matsuura, G. Z. Ye, Y. Mizukami, M. Shimozawa, K. Matsubayashi, M. Yamashita, T. Watashige, S. Kasahara, Y. Matsuda, J. Q. Yan, B. C. Sales, Y. Uwatoko, J. G. Cheng, and T. Shibauchi, Dome-shaped magnetic order competing with high-temperature superconductivity at high pressures in FeSe, *Nat. Commun.* **7**, 12146 (2016).
- [66] T. Gruner, D. J. Jang, Z. Huesges, R. Cardoso-Gil, G. H. Fecher, M. M. Koza, O. Stockert, A. P. Mackenzie, M. Brando, and C. Geibel, Charge density wave quantum critical point with strong enhancement of superconductivity, *Nat. Phys.* **13**, 967 (2017).
- [67] T. Wu, H. Mayaffre, S. Krämer, M. Horvatić, C. Berthier, W. N. Hardy, R. X. Liang, D. A. Bonn, and M. H. Julien, Magnetic-field-induced charge-stripe order in the high-temperature superconductor  $\text{YBa}_2\text{Cu}_3\text{O}_y$ , *Nature (London)* **477**, 191 (2011).
- [68] L. Zhao, C. A. Belvin, R. Liang, D. A. Bonn, W. N. Hardy, N. P. Armitage, and D. Hsieh, A global inversion-symmetry-broken phase inside the pseudogap region of  $\text{YBa}_2\text{Cu}_3\text{O}_y$ , *Nat. Phys.* **13**, 250 (2016).